

Toward Simultaneous Real-time Fluoroscopic and Nuclear Imaging in the Intervention Room¹

Casper Beijst, MSc
Mattijs Elschoot, PhD
Max A. Viergever, DSc
Hugo W. A. M. de Jong, PhD

Purpose:

To investigate the technical feasibility of hybrid simultaneous fluoroscopic and nuclear imaging.

Materials and Methods:

An x-ray tube, an x-ray detector, and a gamma camera were positioned in one line, enabling imaging of the same field of view. Since a straightforward combination of these elements would block the lines of view, a gamma camera setup was developed to be able to view around the x-ray tube. A prototype was built by using a mobile C-arm and a gamma camera with a four-pinhole collimator. By using the prototype, test images were acquired and sensitivity, resolution, and coregistration error were analyzed.

Results:

Nuclear images (two frames per second) were acquired simultaneously with fluoroscopic images. Depending on the distance from point source to detector, the system resolution was 1.5–1.9-cm full width at half maximum, the sensitivity was $(0.6\text{--}1.5) \times 10^{-5}$ counts per decay, and the coregistration error was -0.13 to 0.15 cm. With good spatial and temporal alignment of both modalities throughout the field of view, fluoroscopic images can be shown in grayscale and corresponding nuclear images in color overlay.

Conclusion:

Measurements obtained with the hybrid imaging prototype device that combines simultaneous fluoroscopic and nuclear imaging of the same field of view have demonstrated the feasibility of real-time simultaneous hybrid imaging in the intervention room.

©RSNA, 2015

Online supplemental material is available for this article.

¹From the Department of Radiology and Nuclear Medicine (C.B., M.E., H.W.A.M.d.J.) and Image Sciences Institute (C.B., M.A.V.), University Medical Center Utrecht, Mail E01.132, PO Box 85500, 3508GA Utrecht, the Netherlands. Received December 2, 2014; revision requested January 23, 2015; revision received February 23; accepted March 30; final version accepted April 9. Supported by the Dutch Technology Foundation STW (project number 12977).

Address correspondence to C.B. (e-mail: cbeijst@umcutrecht.nl).

©RSNA, 2015

One of the major advances in oncologic imaging in the past decades has been the development of hybrid imaging modalities, including single photon emission computed tomography (SPECT)/computed tomography (CT) and positron emission tomography (PET)/CT (1,2), which show both anatomic and molecular information. To date, no real-time hybrid imaging modalities for interventional purposes have been developed that combine simultaneously acquired nuclear and anatomic images. The intraoperative availability of molecular information may be achieved by registering preoperative SPECT or PET data to intraoperative fluoroscopic or CT data (3). However, the registration of the nonrigid target organs remains a challenge, and the preoperative images may not represent the actual activity distribution. Alternatively, diagnostic hybrid systems can be used in the intervention room, but most hybrid diagnostic systems, such as PET/CT systems, do not allow simultaneous acquisition of nuclear and anatomic images, and the closed gantry setup is not ideal for interventional applications (4,5). Therefore, gamma probes and handheld gamma cameras are often used to perform radio-guided procedures, although interpretation of the information about the radioactivity distribution can be complex for lack of coregistered anatomic information.

We present an interventional fluoroscopic and nuclear imaging system that is capable of combined simultaneous fluoroscopic and nuclear imaging,

Advances in Knowledge

- Measurements with our concept device demonstrated that real-time simultaneous hybrid imaging in the intervention room is feasible.
- Depending on the distance from point source to detector, the system resolution was 1.5–1.9-cm full width at half maximum, the sensitivity was $(0.6\text{--}1.5) \times 10^{-5}$ counts per decay, and the coregistration error was -0.13 to 0.15 cm.

producing intrinsically registered hybrid images. Procedures that can potentially benefit from real-time simultaneous hybrid imaging include selective internal radiation therapy and liver radioembolization (6–8), biopsies (3,9), tumor resections (10), and radiofrequency ablations (11). Real-time functional imaging in concert with anatomic imaging would provide the physician with valuable information during the procedure, thereby improving therapeutic efficiency. As an example, the selective internal radiation therapy procedure may be drastically shortened if direct feedback about extrahepatic activity of the radionuclide is available during injection of the therapeutic microspheres in the intervention room.

The goal of this study was to investigate the technical feasibility of hybrid simultaneous fluoroscopic and nuclear imaging.

Materials and Methods

The gamma camera used in this study was provided by Siemens Healthcare, Erlangen, Germany. The authors had control of the data and the information submitted for publication.

Device Design

The x-ray tube, the gamma camera, and the x-ray detector were placed in one line to enable imaging of the same field of view. However, straightforward geometric configurations of the gamma camera and the C-arm in one line would block the line of sight of either one of the modalities. This problem was solved by placing the gamma camera behind the x-ray tube, and four pinholes were created around the x-ray tube to create stereoscopic pinhole views of the field of view. The pinholes were positioned such that the center of the three-dimensional

Implication for Patient Care

- Real-time functional imaging in concert with anatomic imaging would provide the physician with valuable information during the procedure and thereby improve therapeutic efficiency.

field of view was imaged through all four pinholes (Fig 1).

Prototype

A prototype of the interventional fluoroscopic and nuclear imaging system was built; see Figure 1. A Diacam gamma camera (Siemens Healthcare, Erlangen, Germany) with a 9.5-mm NaI(Tl) scintillation crystal was used to acquire nuclear images, and a BV29 C-arm (Philips Healthcare, Best, the Netherlands) with a 22.9-cm image intensifier was used to acquire fluoroscopic images. Four 5-mm lead pinholes were fabricated and placed next to the x-ray tube. Lead shielding of at least 4-mm thickness was applied around the pinholes and the gamma camera to prevent uncollimated photons from interacting with the scintillation crystal. The dimensions of the prototype are given in the Table. Scintigraphic images were acquired on a 256×256 grid with $2.4 \times 2.4\text{-mm}^2$ pixel size. The gamma camera was subdivided into four quadrants—one 128×128 quadrant for each individual pinhole (Fig 2).

Reconstruction, Coregistration, and Overlay

The positioning of the pinhole collimators allows conversion of the pinhole projections into one nuclear image that overlaps with the fluoroscopic image.

In the past, several techniques have been developed to merge information from a limited number of projections into a single image (12). Tomosynthesis

Published online before print

10.1148/radiol.2015142749 Content code: **NM**

Radiology 2016; 278:232–238

Author contributions:

Guarantors of integrity of entire study, C.B., H.W.A.M.d.J.; study concepts/study design or data acquisition or data analysis/interpretation, all authors; manuscript drafting or manuscript revision for important intellectual content, all authors; approval of final version of submitted manuscript, all authors; agrees to ensure any questions related to the work are appropriately resolved, all authors; literature research, C.B., H.W.A.M.d.J.; experimental studies, C.B., M.E., H.W.A.M.d.J.; statistical analysis, H.W.A.M.d.J.; and manuscript editing, all authors

Conflicts of interest are listed at the end of this article.

Figure 1

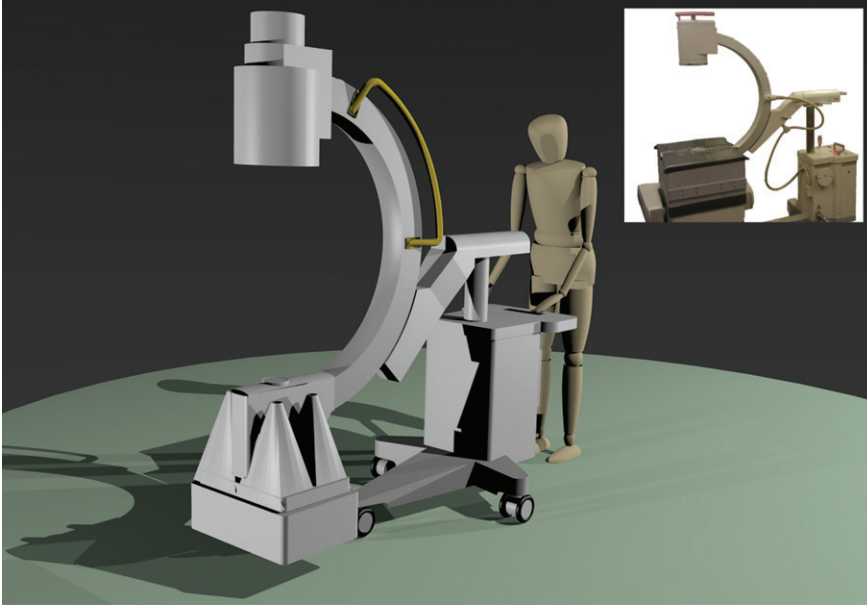


Figure 1: Rendering and prototype of the interventional fluoroscopic and nuclear imaging system.

Dimensions of the Hybrid C-Arm

Measurement	Distance (cm)
Distance from the pinhole to the sodium iodide crystal	38.7
Distance from the pinhole to the x-ray detector	79.0
Diameter of the image intensifier	22.9
Pinhole diameter	0.5

is now often applied as an extension to mammography (13–15).

For conversion, first the three-dimensional activity distribution was iteratively estimated from the four pinhole projections by using a maximum-likelihood expectation-maximization reconstruction algorithm. Resolution recovery was incorporated in both the forward-projection and the back-projection step of the reconstruction algorithm by means of analytical determination of the point spread function, taking into account the finite dimensions of the cone opening and pinhole edge penetration (16–18).

Next, the three-dimensional activity distribution was forward projected along the direction of the x-ray photons, creating a nuclear image obtained from the same point of view as the x-ray tube. Subsequently, multimodality images were created by showing fluoroscopic images in grayscale and nuclear images in color overlay.

Fluoroscopic images were acquired at 25 frames per second and corrected for image nonlinearities, including pin-cushion and barrel distortions (19). Nuclear images were acquired at a rate of two frames per second. Results of simultaneous fluoroscopic and nuclear acquisitions were visualized at five frames per second. For visual purposes, the nuclear images were supersampled by means of interpolation to match the spatial and temporal sizes of the visualized fluoroscopic images (20).

Image Quality Characterization

Measurements were performed with a technetium 99m (^{99m}Tc) point source placed on 30 different positions between 1 and 30 cm from the x-ray detector. The point source was positioned on the central line through the x-ray tube and the x-ray detector. To create a phantom visible

Figure 2

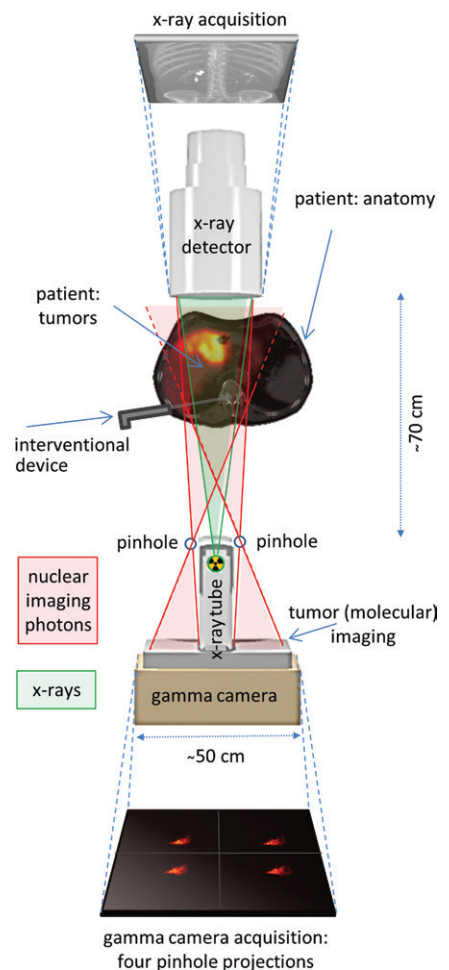
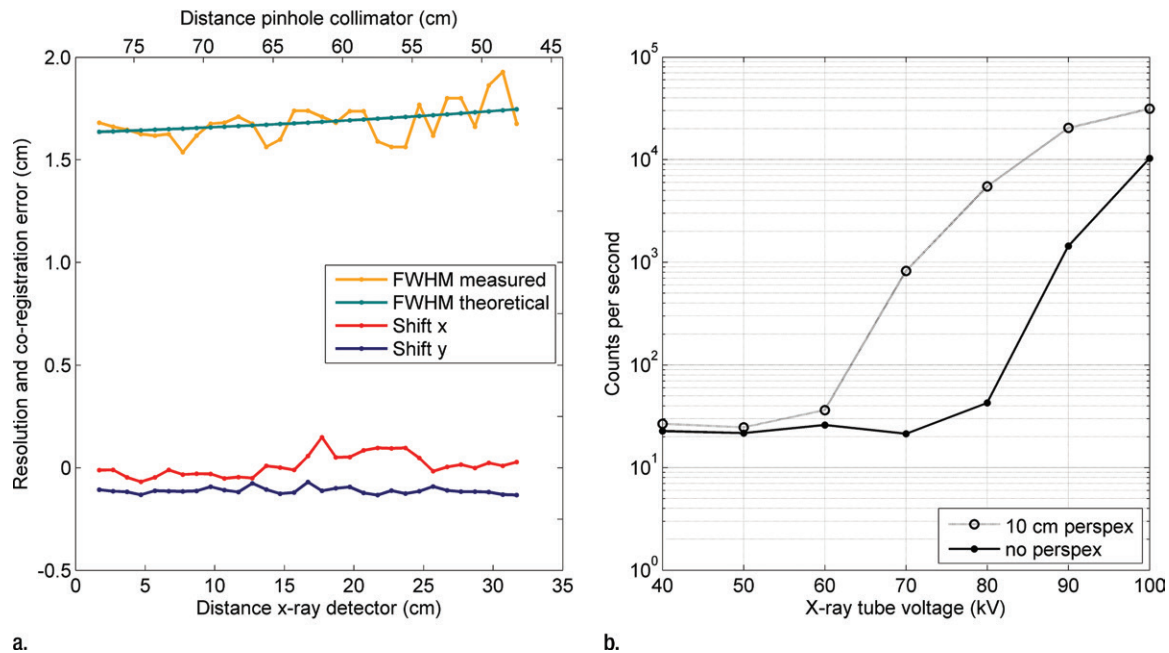


Figure 2: Schematic drawing of the hybrid C-arm shows the field of view of the pinhole collimator and the x-ray photons.

for both modalities, a 3-mm spherical cavity in a polymethyl methacrylate cylinder was filled with 2.0 MBq of ^{99m}Tc . A 60-second acquisition was performed for each location of the point source, using a 15% energy window centered at 140 keV. The measured projections were used to reconstruct a volume of $64 \times 64 \times 64$ voxels with a $4.8 \times 4.8 \times 4.8\text{-mm}^3$ voxel size. A reconstruction of the nuclear image was performed by using 10 maximum-likelihood expectation-maximization iterations. Fluoroscopic images were acquired with a 45-kV tube voltage and 0.20-mA tube current. Subsequently, the full width at half maximum of the reconstructed and coregistered nuclear

Figure 3



a.

b.

Figure 3: Graphs of quantitative performance measurements of the prototype show (a) the resolution and the coregistration error of the nuclear projection image as a function of distance from the x-ray detector and (b) the number of counts measured in the gamma camera energy window as a function of x-ray tube voltage. *FWHM* = full width at half maximum, *perspex* = polymethyl methacrylate.

projection image, the sensitivity of the gamma camera with collimator, and the overlap error between both modalities were calculated. Theoretical values of the resolution were calculated for comparison (21). The coregistration error was determined by calculating the distance between the centers of gravity of the fluoroscopic image and the nuclear image.

Intermodal Spillover

X-ray photons may undesirably be detected by the gamma camera. For instance, this can be directly due to insufficient shielding or through the pinholes via back-scattering. Two sets of measurements were performed by using x-ray tube voltages between 40 and 100 kV: The first with an empty field of view (with air) and the second with 10 cm of polymethyl methacrylate in front of the x-ray detector, acting as a scatter medium. The scatter material consisted of 10 stacked in-house-manufactured $40 \times 40 \times 1$ -cm polymethyl methacrylate plates with a density of 1.18 g/cm^3 . The x-ray tube was switched on

during the entire 5-second scintigraphic acquisition.

Phantoms

A syringe with a droplet (0.02 mL) of 25.9 MBq of ^{99m}Tc solution was moved through the combined field of view of both modalities. The gamma camera was used to acquire 60 frames of 500 msec. The maximum-likelihood expectation-maximization algorithm with three iterations was used to reconstruct the three-dimensional activity distribution for each time frame. Fluoroscopic images were acquired with a 50-kV tube voltage and 0.44-mA tube current.

Subsequently, the IEC NEMA 2007 phantom (PTW, Freiburg, Germany) with two of six spheres (17 mm and 37 mm) filled with 3.7 MBq per milliliter was rotated under an angle of 16° in the combined field of view of both modalities. The size of the anthropomorphic phantom was 30.5 cm (long axis) \times 24.1 cm (short axis) \times 24.1 cm (height). The background compartment was not filled with water to enhance the

image contrast for assessment of intermodal coregistration. The gamma camera was used to acquire 100 frames of 500 msec. During the entire acquisition, fluoroscopic images were acquired with a 44-kV tube voltage and 0.16-mA tube current.

Results

Quantitative Analysis

The results of ^{99m}Tc point source measurements to analyze resolution, sensitivity, and coregistration errors are shown in Figure 3a. The full width at half maximum of nuclear point source images was in the range 1.5–1.9 cm. The coregistration error was between -0.13 and 0.15 cm , which is roughly an order of magnitude smaller than the resolution of the nuclear image. The sensitivity was $(0.6\text{--}1.5) \times 10^{-5}$ counts per decay.

Intermodal Spillover

Figure 3b shows the amount of counts in the 15% energy window centered at

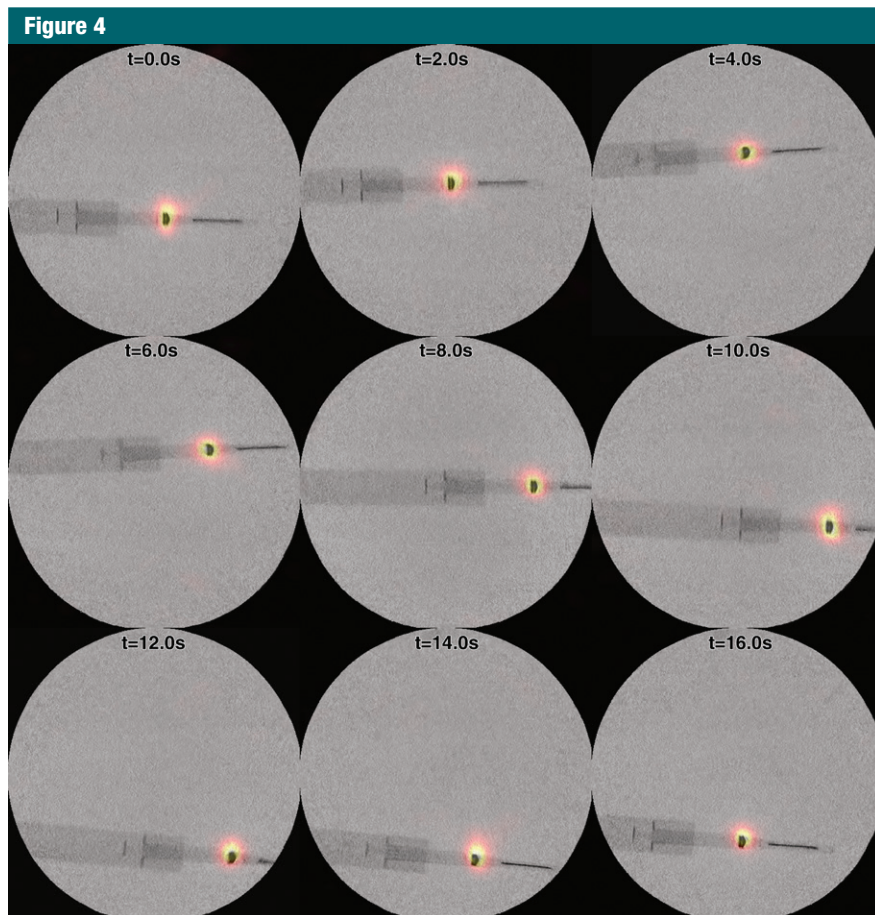


Figure 4: Montage of frames from a simultaneous hybrid acquisition (Movie 1 [online]) of a syringe with 25.9 MBq of ^{99m}Tc , with fluoroscopic images in grayscale and nuclear images in color overlay. $t =$ time, $s =$ seconds.

140 keV for different values of the x-ray tube current. The measurements show that the amount of counts increased rapidly as the tube voltage increased beyond 60 kV (with scatter material) and 80 kV (without scatter material).

Phantoms

A syringe with 25.9 MBq of ^{99m}Tc was moved through the combined field of view, as shown in Figure 4 and Movie 1 (online). With good spatial and temporal overlap of both modalities, a montage of fluoroscopic images is shown in grayscale and nuclear images in color overlay. No artifacts could be detected on the fluoroscopic images, which shows that fluoroscopic imaging is unaffected by the presence of the radioactive tracer, the pinholes, or the

gamma camera. Similar results were obtained by using an IEC NEMA 2007 phantom (PTW) with 17-mm and 37-mm spheres filled with 3.7 MBq per milliliter. A montage of acquired hybrid images is shown in Figure 5 and Movie 2 (online).

Discussion

Real-time hybrid imaging promises to improve radio-guided procedures. In this study, measurements with a prototype setup demonstrate that real-time simultaneous fluoroscopic and nuclear imaging of the same field of view is feasible. This was achieved without adding constraints to the traditional setup of the C-arm, to the fluoroscopic imaging structure, and to the interventional setup.

The coregistration error was shown to be an order of magnitude smaller than the in-plane resolution of the nuclear image. The hybrid fluoroscopic and nuclear images demonstrated good spatial and temporal overlap.

The purpose of the hybrid C-arm is not to compete with diagnostic hybrid imaging devices in terms of image parameters, such as resolution and contrast. The proposed system is rather aimed at guiding interventional oncologic procedures. The intrinsic spatial coregistration of the fluoroscopic and nuclear images is a great advantage in supporting the dynamic procedures in the intervention room.

Constructing a real prototype can prove the technical feasibility of a system, but it may also reveal unforeseen obstacles. Prototype measurements showed substantial spillover of x-rays onto the nuclear images, even at tube potential settings well below the lower energy threshold of the nuclear imaging (126 keV). Pileup effects in the gamma camera can cause multiple x-ray photons to be detected as a single gamma photon, potentially causing x-ray photons to be counted in the energy window. Possible solutions to the spillover problem include antisynchronization of the nuclear acquisition with pulsed fluoroscopy (22). Assuming that fluoroscopic images are acquired with a frequency of five frames per second and a pulse width of 5 msec, only 2.5% of the counts would theoretically be lost to prevent detection of possibly scattered x-rays in the gamma camera energy window. Furthermore, the effects of x-ray photon pileup can be overcome by using detectors with a higher temporal resolution than detectors equipped with a NaI(Tl) scintillation crystal, such as a lutetium yttrium orthosilicate or LaBr_3 scintillation crystal with a much shorter decay time (23,24).

Since the C-arm used did not allow pulsed fluoroscopy to prevent the spillover, the measurements of the NEMA phantom (PTW) were performed without water in the background compartment to limit the effects of back-scattered x-ray photons.

Figure 5

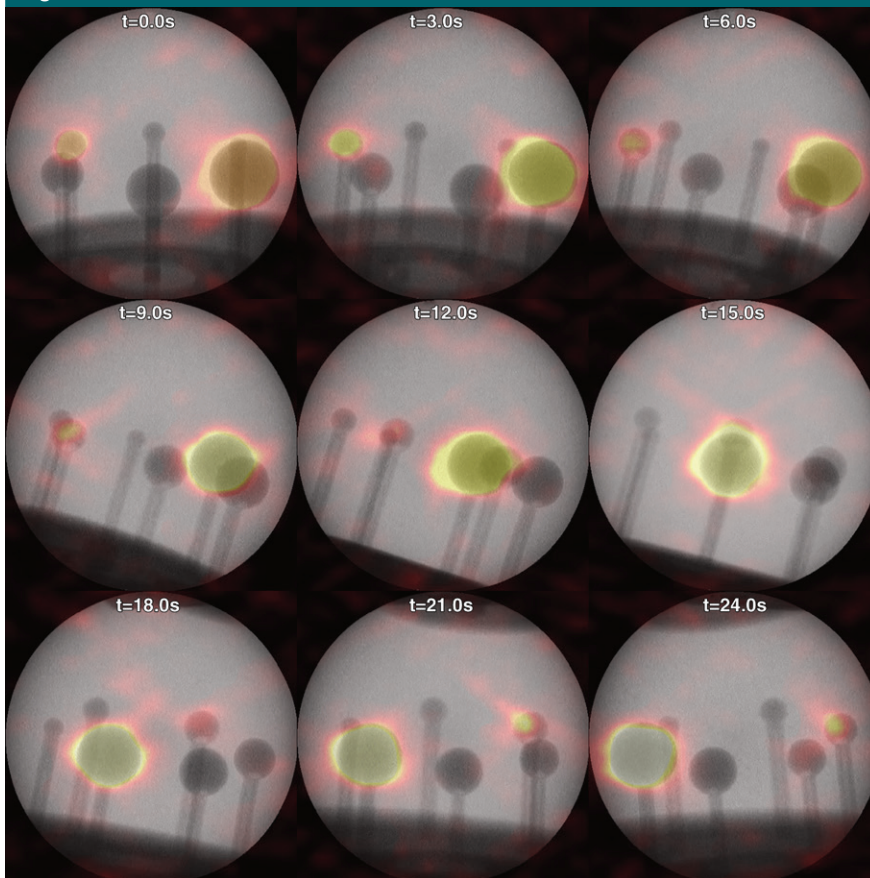


Figure 5: Montage of frames from a simultaneous hybrid acquisition (Movie 2 [online]) of a ^{99m}Tc phantom with 3.7 MBq per milliliter, with fluoroscopic images in grayscale and nuclear images in color overlay. $t =$ time, $s =$ seconds.

In this prototype, which was set up by using a standard desktop personal computer and software not optimized for speed, the mean postprocessing time for a single visualization frame was approximately 3 seconds, which allowed only retrospective image evaluation. Several groups have shown that substantial acceleration can be achieved by parallel processing on graphic processing units (25). Therefore, we believe real-time processing is feasible when optimized hardware and software are used.

Future research will be aimed at improving the image quality while maintaining the system's capability of simultaneous hybrid imaging. Larger digital flat-panel x-ray detectors capable of imaging the entire patient may be

more practical for clinical procedures than the relatively small image intensifier with a diameter of 22.9 cm used for the prototype. Moreover, the application of (a) smaller detectors for nuclear imaging that require less shielding and (b) parallel hole collimators may improve sensitivity and resolution and allow a flexible lightweight design. The resolution and sensitivity required to provide the physician with clinically relevant information will strongly depend on the clinical application. This will be assessed in future research by using the hybrid C-arm in preclinical settings, such as radioembolization.

In conclusion, a novel hybrid imaging prototype that combines simultaneous fluoroscopic and nuclear imaging of the same field of view has been

proposed. Measurements with our concept device demonstrated that real-time hybrid imaging in the intervention room is feasible.

Acknowledgments: The authors thank R. L. P. van Veen, PhD, for critically reviewing the manuscript and Z. Nouwen, BEng, for technical support.

Disclosures of Conflicts of Interest: C.B. Activities related to the present article: author received a grant from ITEA. Activities not related to the present article: disclosed no relevant relationships. Other relationships: disclosed no relevant relationships. M.E. Activities related to the present article: author received a grant from STW and nonfinancial support in the form of equipment from Siemens Healthcare. Activities not related to the present article: disclosed no relevant relationships. Other relationships: disclosed no relevant relationships. M.A.V. Activities related to the present article: author received a grant from ITEA2. Activities not related to the present article: disclosed no relevant relationships. Other relationships: disclosed no relevant relationships. H.W.A.M.d.J. Activities related to the present article: disclosed no relevant relationships. Activities not related to the present article: disclosed no relevant relationships. Other relationships: author has a patent pending.

References

1. Basu S, Alavi A. SPECT-CT and PET-CT in oncology—an overview. *Curr Med Imaging Rev* 2011;7(3):202–209.
2. Delbeke D, Sandler MP. The role of hybrid cameras in oncology. *Semin Nucl Med* 2000;30(4):268–280.
3. Tatli S, Gerbaudo VH, Mamede M, Tuncali K, Shyn PB, Silverman SG. Abdominal masses sampled at PET/CT-guided percutaneous biopsy: initial experience with registration of prior PET/CT images. *Radiology* 2010;256(1):305–311.
4. Kl-aeser B, Mueller MD, Schmid RA, Guevara C, Krause T, Wiskirchen J. PET-CT-guided interventions in the management of FDG-positive lesions in patients suffering from solid malignancies: initial experiences. *Eur Radiol* 2009;19(7):1780–1785.
5. Tatli S, Gerbaudo VH, Feeley CM, Shyn PB, Tuncali K, Silverman SG. PET/CT-guided percutaneous biopsy of abdominal masses: initial experience. *J Vasc Interv Radiol* 2011;22(4):507–514.
6. Gulec SA, Fong Y. Yttrium 90 microsphere selective internal radiation treatment of hepatic colorectal metastases. *Arch Surg* 2007;142(7):675–682.
7. Salem R, Thurston KG. Radioembolization with ^{90}Y yttrium microspheres: a state-of-

- the-art brachytherapy treatment for primary and secondary liver malignancies. Part 1: technical and methodologic considerations. *J Vasc Interv Radiol* 2006;17(8):1251–1278.
8. Vente MA, Wondergem M, van der Tweel I, et al. Yttrium-90 microsphere radioembolization for the treatment of liver malignancies: a structured meta-analysis. *Eur Radiol* 2009;19(4):951–959.
 9. Kobayashi K, Bhargava P, Raja S, et al. Image-guided biopsy: what the interventional radiologist needs to know about PET/CT. *RadioGraphics* 2012;32(5):1483–1501.
 10. Vidal-Sicart S, Rioja ME, Paredes P, Keshgar MR, Valdés Olmos RA. Contribution of perioperative imaging to radioguided surgery. *Q J Nucl Med Mol Imaging* 2014;58(2):140–160.
 11. Wood BJ, Locklin JK, Viswanathan A, et al. Technologies for guidance of radiofrequency ablation in the multimodality interventional suite of the future. *J Vasc Interv Radiol* 2007;18(1 Pt 1):9–24.
 12. Crowther RA, Amos LA, Finch JT, De Rosier DJ, Klug A. Three dimensional reconstructions of spherical viruses by fourier synthesis from electron micrographs. *Nature* 1970;226(5244):421–425.
 13. Dobbins JT 3rd, Godfrey DJ. Digital x-ray tomosynthesis: current state of the art and clinical potential. *Phys Med Biol* 2003;48(19):R65–R106.
 14. Grant DG. Tomosynthesis: a three-dimensional radiographic imaging technique. *IEEE Trans Biomed Eng* 1972;19(1):20–28.
 15. Yaffe MJ, Mainprize JG. Digital tomosynthesis: technique. *Radiol Clin North Am* 2014;52(3):489–497.
 16. Bal G, Acton PD. Analytical derivation of the point spread function for pinhole collimators. *Phys Med Biol* 2006;51(19):4923–4950.
 17. Metzler SD, Bowsher JE, Greer KL, Jaszczak RJ. Analytic determination of the pinhole collimator's point-spread function and RMS resolution with penetration. *IEEE Trans Med Imaging* 2002;21(8):878–887.
 18. Vanhove C, Andreyev A, Defrise M, Nuyts J, Bossuyt A. Resolution recovery in pinhole SPECT based on multi-ray projections: a phantom study. *Eur J Nucl Med Mol Imaging* 2007;34(2):170–180.
 19. Wallace WA, Johnson F. Detection and correction of geometrical distortion in x-ray fluoroscopic images. *J Biomech* 1981;14(2):123–125.
 20. Gould RG, Lipton MJ, Mengers P, Dahlberg R. Investigation of a video frame averaging digital subtraction fluoroscopic system. *Proc SPIE* 1981;0314:184–190.
 21. Metzler SD, Bowsher JE, Smith MF, Jaszczak RJ. Analytic determination of pinhole collimator sensitivity with penetration. *IEEE Trans Med Imaging* 2001;20(8):730–741.
 22. Plewes DB, Vogelstein E. Grid controlled x-ray tube switching time: implications for rapid exposure control. *Med Phys* 1984;11(5):693–696.
 23. Lewellen TK. Recent developments in PET detector technology. *Phys Med Biol* 2008;53(17):R287–R317.
 24. Peterson TE, Furenlid LR. SPECT detectors: the Anger Camera and beyond. *Phys Med Biol* 2011;56(17):R145–R182.
 25. Eklund A, Dufort P, Forsberg D, LaConte SM. Medical image processing on the GPU—past, present and future. *Med Image Anal* 2013;17(8):1073–1094.